Heliyon

Received:
4 November 2017
Revised:
5 February 2018
Accepted:
2 April 2018

Cite as: Richa Bhardwaj, Amardeep Bharti, Jitendra P. Singh, Keun Hwa Chae, Navdeep Goyal, Sanjeev Gautam. Structural and electronic investigation of ZnO nanostructures synthesized under different environments. Heliyon 4 (2018) e00594.
doi: 10.1016/j.heliyon.2018.e00594

Structural and electronic investigation of ZnO nanostructures synthesized under different environments

Richa Bhardwaj [a], **Amardeep Bharti** [a], **Jitendra P. Singh** [b], **Keun Hwa Chae** [b,*], **Navdeep Goyal** [a], **Sanjeev Gautam** [c,*]

[a] *Department of Physics, Panjab University, Chandigarh, 160014, India*

[b] *Advanced Analysis Center, Korea Institute of Science and Technology, Seoul, 02792, South Korea*

[c] *Dr. S.S. Bhatnagar Institute of Chemical Engineering & Technology, Panjab University, Chandigarh, 160014, India*

[*] Corresponding authors.

E-mail addresses: khchae@kist.re.kr (K.H. Chae), sgautam@pu.ac.in (S. Gautam).

Abstract

An explicit study of comparison on the basis of structure and electronic properties of ZnO nanostructures was discussed. ZnO synthesized by sol-gel and hydrothermal method without using any surfactant leads to the formation of two different morphologies. Rietveld crystal structure refinement of X-ray diffraction patterns confirmed the wurtzite structure of both samples. Raman spectra also confirmed the wurtzite phase formation and improved crystallinity in sample synthesized by hydrothermal route that are concurrent with results obtained from X-ray diffraction. Field-emission scanning electron microscopy revealed the formation of ZnO spherical nanoparticle structure for sol-gel method and flower like μ-structure for ZnO prepared through hydrothermal route. Williamson-Hall equations applied to study the strain and stress parameters present in the material, show the decrease in their values as the crystal size increases. Energy band gap is calculated using diffused reflectance spectroscopy. Near-edge X-ray absorption fine-structure measurements at O *K*- and Zn $L_{3,2}$- edges simulated with FEFF9.05 code confirmed the presence of oxygen vacancies. Further

https://doi.org/10.1016/j.heliyon.2018.e00594

extended x-ray absorption fine-structure revealed a similar local atomic structure for both samples despite having different morphologies.

Keywords: Condensed matter physics, Nanotechnology, Materials science

1. Introduction

In recent years, morphology dependent applications of nanomaterials are under investigation [1, 2, 3]. Change in morphology of nanomaterials open up pathways for utilizing these nanomaterials for such applications, which could not be realized for spherical nanoparticles [4, 5]. Thus numbers of oxide materials are being explored to establish correlation among morphology and properties. One such example is ZnO that has been reported to be the richest family in terms of different morphologies and material structures [6]. Depending upon morphology, ZnO has vast area of application in electronics [7], sensing [8], magnetic [9], catalytic [10], and solar cell devices [11]. Several research groups have synthesized ZnO nanostructures that include nanowires, nanotubes, nanobelts, nanorods by different available methods such as physical and chemical deposition method [6], spray pyrolysis [12], sol-gel method [13], and hydrothermal method [14]. These studies envisage that ZnO nanostructure growth morphology is strongly influenced by the route chosen for synthesis and surrounding environment of the process [15, 16]. Wang *et al.* [17] synthesized hierarchical flower-like ZnO nanostructures by one-step solution route and demonstrated the role of OH^- ions in formation of flower-like nanostructures.

While investigating the nanostructure properties, crystallite size is ordinarily obtained from X-ray diffraction (XRD) pattern by using Debye-Scherrer formula of size calculation but it lacks the contribution from lattice strain parameter that also leads to XRD peak broadening. Strain occurs in material due to crystal imperfections and dislocations. Moreover along with crystal size, presence of vacancies and metal-oxide bond length equally play a crucial role in determining the physical properties. The complete knowledge of these parameters is of utmost importance. Thus in order to have necessary and appropriate understanding, Williamson-Hall (W-H) method is used to extract the size parameters. W-H method is simplified approach that allows one to quantitatively determine lattice strain from XRD peak broadening. Uniform deformation model (UDM), Uniform stress deformation model (USDM) and Uniform deformation energy density model (UDEDM) are used to approximate crystal size, lattice strain, and stress and energy density parameters [18]. These models are derived from the modified equation of W-H method. Similarly, work on evaluating metal-oxide bond length, presence of vacancies such as oxygen and Zinc vacancies have also been reported. Xiaodong *et al.* [19] presented theoretical approach to the role of oxygen vacancies in intrinsic and defect of ZnO crystal by considering $2 \times 2 \times 2$ ZnO supercell

https://doi.org/10.1016/j.heliyon.2018.e00594

having 16 zinc and 16 oxygen atoms. Some research groups used synchrotron based X-ray absorption spectroscopy (XAS) technique to attain metal-oxide bond length and vacancies present in materials [20]. Akgul *et al.* [21] synthesized doped ZnO nanocomposites and provided the qualitative information about the different bond lengths through XAS measurements, but till date limited theoretical and experimental reports are available that focuses on change in local electronic/atomic structure of absorbing atom with the change in morphology. Moreover, the electronic structural properties using XAS and Reitveld's refinements analysis have been rarely compared for these process by other authors.

In this paper, ZnO was synthesized by two different routes i.e., sol-gel and hydrothermal method. The synthesis route decides the chemical and physical properties of the samples, which are minutely discussed for their crystallinity, surface morphology and strain. We report the comparative study obtained in terms of crystal size, metal-oxide bond length and vacancies present in these two synthesized systems. The density functional theory (DFT) based FEFF 9.0.5 has also been used to simulate the near-edge X-ray absorption fine-structure (NEXAFS) and extended x-ray absorption fine-structure (EXAFS) spectra.

2. Experimental

2.1. Synthesis of ZnO nanostructures

In the synthesis process, chemicals were of analytical grade and used as received.

Sol-gel method: To synthesize ZnO nanoparticles, 0.1M $Zn(CH_3COO)_2 \cdot 2H_2O$ was dissolved in 100 ml de-ionized (DI) water. To this solution, 0.1M aqueous KOH prepared in DI-water was added drop by drop under continuous magnetic stirring (pH $\approx$ 9) at room temperature till the formation of milky precipitates (gel). This gel was then grouped into two, named as R1 and R2 for comparative study under different synthesis environment (R1 and R2 will be used thereafter). R1 was centrifuged at 3000 rpm and washed many times, first with DI water and then with isopropyl alcohol. It was dried at 80 °C for 6 h in oven and grounded with mortar pestle into a fine powder.

Hydrothermal method: Following the above procedure, R2 was transferred into teflon-lined stainless steel autoclave; half filled with isopropyl and maintained at 150 °C for 24 h. The resulting product was centrifuged and washed in the same manner as described previously. It was sintered at 400 °C for one hour and allowed to cool down slowly to room temperature. Finally it was also grounded to a fine powder. The schematic of synthesis procedure is shown in Fig. 1.

https://doi.org/10.1016/j.heliyon.2018.e00594

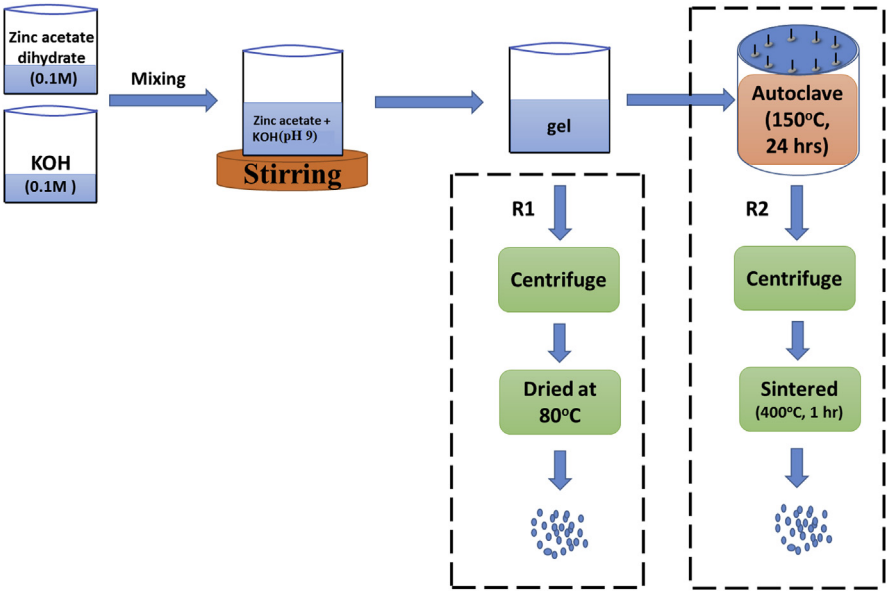

Fig. 1. Schematic representation of synthesis process: Sol-gel (R1) and hydrothermal (R2) methods.

2.2. Characterization

The crystallinity of synthesized samples was determined through X-ray diffraction (XRD, Panalytical's X'Pert Pro) having Cu K_α radiation ($\lambda = 0.1541$ nm) at Bragg's angle ranging from 20^o to 90^o with 1^o per minutes for better resolution. Morphological study was done using FE-SEM (FEI Quanta FEG 200 HRSEM). The Raman scattering measurements were performed using Ranishaw InVia Raman microscope under the excitation by 514 nm argon-ion laser at 50 mW power. UV-diffuse reflectance spectroscopy (UV-2600 SHIMADZU) was performed to obtain the energy band gap. Near-edge X-ray absorption fine-structure (NEXAFS) measurements at O *K*- and Zn $L_{3,2}$- edges were performed on both the samples at 10D(XAS-KIST) beamline and extended X-ray absorption fine-structure (EXAFS) measurements for Zn *K*- edge was done at 1D XRS KIST-PAL beamline of Pohang Accelerator Laboratory, South Korea. The details of NEXAFS and EXAFS measurements are described elsewhere [22].

2.3. Simulation details

Fullprof software was used for Rietveld refinement of XRD data [23]. NEXAFS and EXAFS spectra were simulated for the wurtzite model using software Athena and Artemis (FEFF ver 9.05) code developed by J.J. Rehr based on real space full multiple-scattering theory (FMS) for different experimental parameters to investigate the electronic structure changes [24, 25].

https://doi.org/10.1016/j.heliyon.2018.e00594

3. Results and discussion

3.1. Structure and phase formation

Fig. 2 shows refined XRD patterns for R1 and R2 by considering P*63mc* space group. Results confirmed the presence of wurtzite structure in both samples. In the refinement of wurtzite ZnO with Zn at (1/3,2/3,0) and O at (1/3,2/3,u), pseudo-voigt function has been taken into account in describing the Bragg shape.

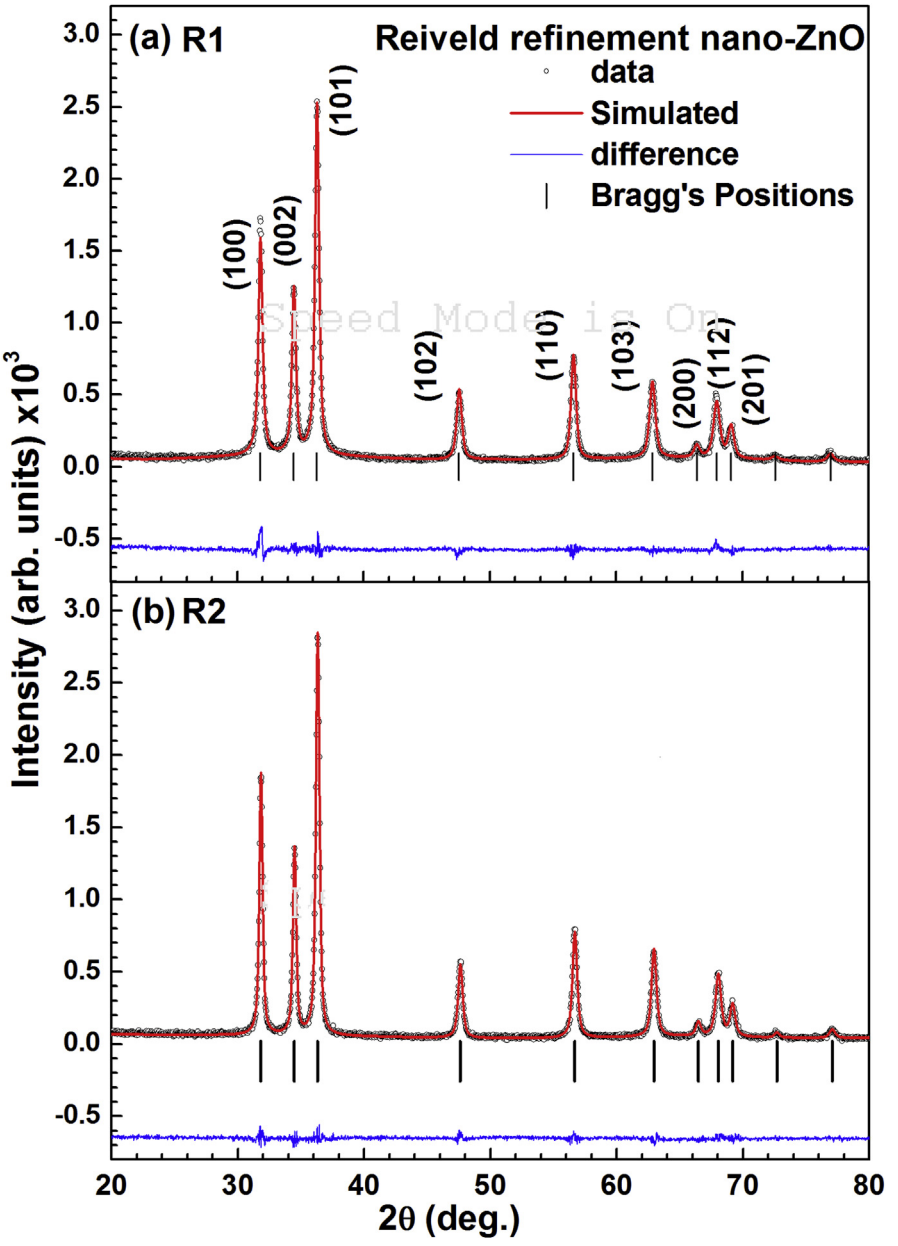

Fig. 2. Rietveld refined XRD pattern of (a) R1 and (b) R2, where blue lines represents the difference (residue) between observed and fitted data points.

https://doi.org/10.1016/j.heliyon.2018.e00594

Final structure obtained after refinement was evaluated by various *R* parameters (reliability parameters) and smallness of χ^2 (fitness factor), which is the difference between observed and fitted data. Fig. 2 shows graph for R1 and R2, in which observed and simulated data were matched with least possible value of χ^2 that came out to be less than 1.5. The various reliability parameters that reveal the fitting quality of experimental data and lattice constants were listed in Table 1. Values obtained were found to be consistent as reported in literature [26]. Further we calculated *c/a* and wurtzite parameter *u*, which is defined as the relative displacement between Zn and O sub-lattices along the *c-axis*. These values deviate from the standard values for the bulk ZnO (*c/a* and *u* parameters as 1.6333 and 0.375, respectively); this infers that Zn-O bond length is different in *c-axis*. Further Zn-O bond length was calculated using formulae $u \cdot c$ (along *c- axis*) and $[a^2/3 + (1/2 - u)^2 c^2]^{1/2}$ (perpendicular to *c-axis*) [27]. Thus bond distance values calculated for R1 and R2 are 1.9908 Å and 1.9892 Å along c, 1.9745 Å and 1.9743 Å in other direction , respectively.

Micro-Raman analysis of ZnO (R1 and R2) was conducted at room temperature. The vibrational modes of phonons at Γ_{opt} point of Brillouin zone was deduced from the following representation

$$\Gamma_{\text{opt}} = A_1 + E_1 + 2E_2 + 2B_1 \tag{1}$$

In above equation (Eq. (1)), the two polar modes A_1 and E_1 are Raman and infrared active modes, respectively and splits into longitudinal (A_{1L}, E_{1L}) and transverse (A_{1T}, E_{1T}) components. E_2 is nonpolar having two-fold degeneracy ($E_{2(low)}$ and $E_{2(high)}$) and is Raman active only. $E_{2(low)}$ mode is analogues to vibration of Zn sub-lattice,

Table 1. Rietveld refined reliability parameters: Rp (profile factor), Rwp (weighted profile factor), Re (expected weighted profile factor), Rb (Bragg factor), Rf (crystallographic factor) and lattice parameter for R1 and R2.

Parameters	Value for samples	
	R1	R2
Rp (%)	12.7	10.70
Rwp (%)	15.1	13.30
Re (%)	13.6	13.40
Rb (%)	4.70	3.43
Rf (%)	3.85	1.94
X^2	1.23	0.99
a (Å)	3.2517	3.2485
c (Å)	5.2090	5.2033
c/a	1.6019	1.6017
u	0.3822	0.3823

https://doi.org/10.1016/j.heliyon.2018.e00594

whereas $E_{2(high)}$ is associated with oxygen atom and represents the wurtzite phase of material [28]. B_1 is silent mode i.e., both Raman and infrared inactive. The Raman spectrum for R1 was found to have peak at 438.2 ± 1 cm^{-1} and for R2 peaks at approx. 203.9 ± 1 cm^{-1}, 332.4 ± 1 cm^{-1}, 438.2 ± 1 cm^{-1}, and 579.5 ± 1 cm^{-1} were observed as shown in Fig. 3. The peak at 438.2 ± 1 cm^{-1} in both samples was $E_{2(high)}$ corresponding to the presence of crystalline wurtzite phase in ZnO. These results were consistent with the one obtained from XRD. Moreover $E_{2(high)}$ peak for R2 was more improved as compared to R1. The other weak peaks in R2 at 203.9 ± cm^{-1} was due to $E_{2(low)}$ and at 332.4 ± 1 cm^{-1} was attributed to difference in frequency of $E_{2(high)}$ and $E_{2(low)}$. This was supposed to be originated from multiple-phonon scattering phenomenon [29]. These modes occur due to structural disorders in the host matrix. The peak at 579.5 ± 1 cm^{-1} in R2 was due to A_{1L} mode. The result of Raman analysis provided the information regarding the improved crystallinity and structure of ZnO in R2. The morphology of ZnO nanostructures highly depends upon pH, precursor concentration, and temperature of growth. Among these parameters, temperature at which the reaction is operated strongly influences the aspect ratio and morphology [30]. Thus the R2 sample synthesized at different condition from R1 has improved nanostructure and crystallinity.

3.2. Structural and morphological investigation

The crystallite size obtained using Debye-Scherrer formula ($D = k\,\lambda/\beta\cos\theta$, where k is constant, λ is Cu K_α radiation wavelength, β is full width half maxima) was

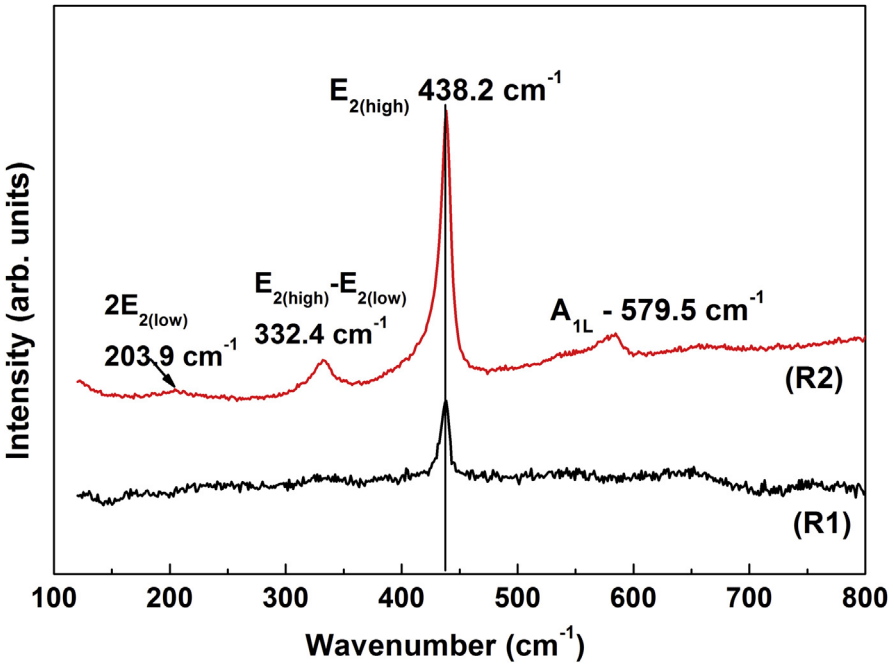

Fig. 3. Raman spectra for R1 and R2, ZnO nanostructure samples.

https://doi.org/10.1016/j.heliyon.2018.e00594

calculated as 23 ± 1 nm for R1 and 26 ± 1 nm for R2. Further ZnO morphologies were studied through FE-SEM micrographs as shown in Fig. 4. It clearly revealed the formation of spherical particles in R1 whereas formation of μ−flower structure took place in ZnO synthesized through hydrothermal method (R2). In R2, some hexagonal ZnO structures have been observed with average side length of 1.62 μm, average width 1.35 μm and angle measurements in degrees (lower portion of Fig. 4). Average size of ZnO μ-flower was about 15 μm whose magnified image was also shown on the right side of Fig. 4.

On the basis of FE-SEM micrographs, it was supposed that the growth mechanism for the formation of structures for R1 and R2 must have involved following three

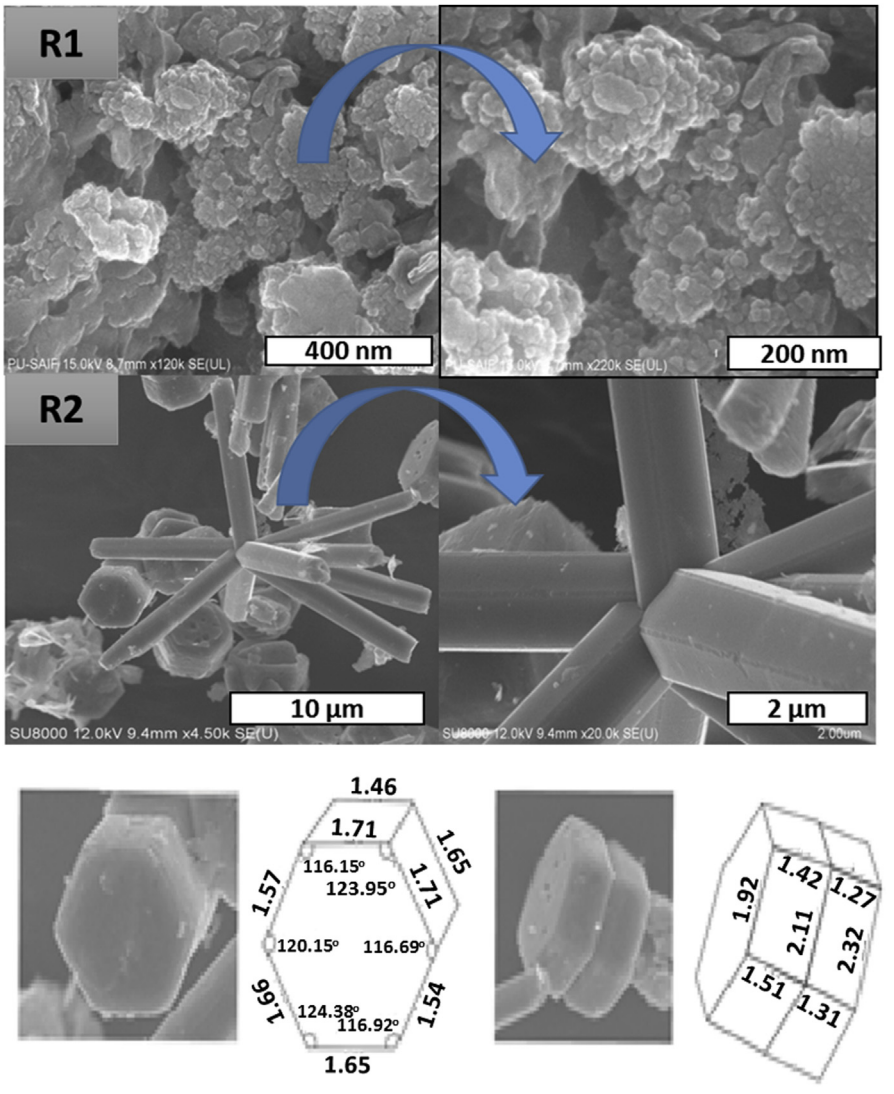

Fig. 4. FE-SEM micrographs for R1 and R2 along with their magnified image on right side and measurement of hexagon structure sides in μm were presented at the bottom of figure.

https://doi.org/10.1016/j.heliyon.2018.e00594

stages as shown in Fig. 5. First stage evolved the formation of $Zn(OH)_2$ white precipitates on titrating aqueous zinc acetate with KOH. Zn^{2+} and OH^- ion concentration strongly influence the growth of $Zn(OH)_2$ nanostructure. On giving the heat treatment to $Zn(OH)_2$, ZnO spherical structures were formed (Eq. (2)). In second stage, crystal was allowed to grow under the controlled environment of autoclave at 150 °C that leads to the decomposition of $Zn(OH)_2$ to ZnO nuclei which was believed to be the elementary unit for the development of final product (Eq. (3)). Moreover if there was an excess of OH^- ions, it would lead to the formation of $[Zn(OH_4)]^{2-}$ which upon dehydration promotes augmentation of ZnO nuclei, respectively. The process was explained through reactions given below [31].

$$Zn(OH)_2 + 2OH^- \rightarrow \left[Zn(OH)_4\right]^{2-} \tag{2}$$

$$\left[Zn(OH)_4\right]^{2-} \leftrightarrow ZnO + H_2O + 2OH^- \tag{3}$$

Under this environment, close packing of ZnO nuclei resulted in the formation of hexagonal structure which was further stacked over one another along *c-axis* forming hexa-poles. ZnO is a polar crystal having two polar surfaces normal to *c-axis*.

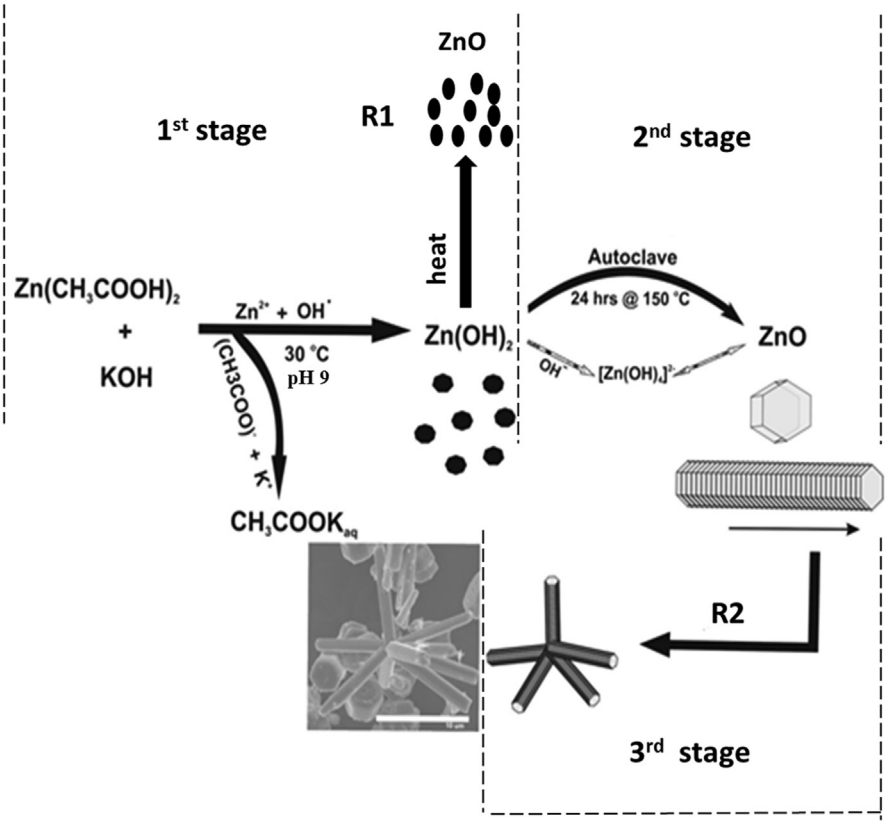

Fig. 5. Three stage growth mechanism for the formation of spherical nanostructure for R1 and μ-flower in case of R2.

https://doi.org/10.1016/j.heliyon.2018.e00594

The top surface is catalytically active Zn(0001) whereas bottom surface is inactive oxygen surface (0001). Thus it helps the top surface to grow energetically in radial direction on the formation of ZnO nuclei. Third stage involves the self-assembly of hexa-poles into three-dimensional μ-flower in order to minimize the surface energy to keep symmetry of the crystal structure [32].

3.3. Strain and stress analysis

W-H plots were studied with its modified equations to evaluate strain, stress and energy density values. Williamson and Hall used convolution to study the effect of both parameters (size and strain) leading to peak broadening.

3.3.1. Uniform deformation model (UDM), uniform stress deformation model (USDM), uniform deformation energy density model (UDEDM)

Broadening of peak due to crystal size, β, (given through Scherrer formula) varies as $1/\mathrm{Cos}\theta$ and due to strain (described as $\beta_e = 4\epsilon\tan\theta$) varies as $\tan\theta$. Thus the W-H equation for total peak broadening becomes

$$\beta_{hkl}\, Cos\ \theta = \frac{k\lambda}{D} + 4\varepsilon\, Sin\theta \tag{4}$$

The Eq. (4) is known as UDM based on the assumption that strain present in the material is uniform in all directions, thus considering the crystal to be isotropic. Similar to UDM, USDM is also based on certain assumptions. So with in elastic limit, Hooke's relation of linear proportionality between stress and strain ($\sigma = Y\varepsilon$, where Y is the Young's Modulus) can be used to determine stress. Following this approach, W-H equation (Eq. (4)) is modified to Eq. (5):

$$\beta_{hkl} Cos\theta = \frac{k\lambda}{D} + \frac{4\sigma Sin\theta}{Y_{hkl}} \tag{5}$$

Young's modulus calculated for hexagonal ZnO nanoparticle was 119 GPa approximately [18]. Another model named UDEDM further used to calculate the approximate energy density of crystal. In UDM, homogeneous isotropic behavior of crystal is taken into consideration that in most of the cases is not true. Thus while considering energy density with in elastic limits, Hooke's law can be given by relation $u = (\varepsilon^2 Y_{hkl})/2$ and W-H Eq. (5) can be rewritten in the form of Eq. (6).

$$\beta_{hkl} Cos\theta = \frac{k\lambda}{D} + \left(4 Sin\theta \left(\frac{2u}{Y_{hkl}}\right)^{\frac{1}{2}}\right) \tag{6}$$

Linear fitted W-H plots were drawn as shown in Fig. 6(a, b and c), whose slope deduced information about strain, stress and energy density and the intercept was

https://doi.org/10.1016/j.heliyon.2018.e00594

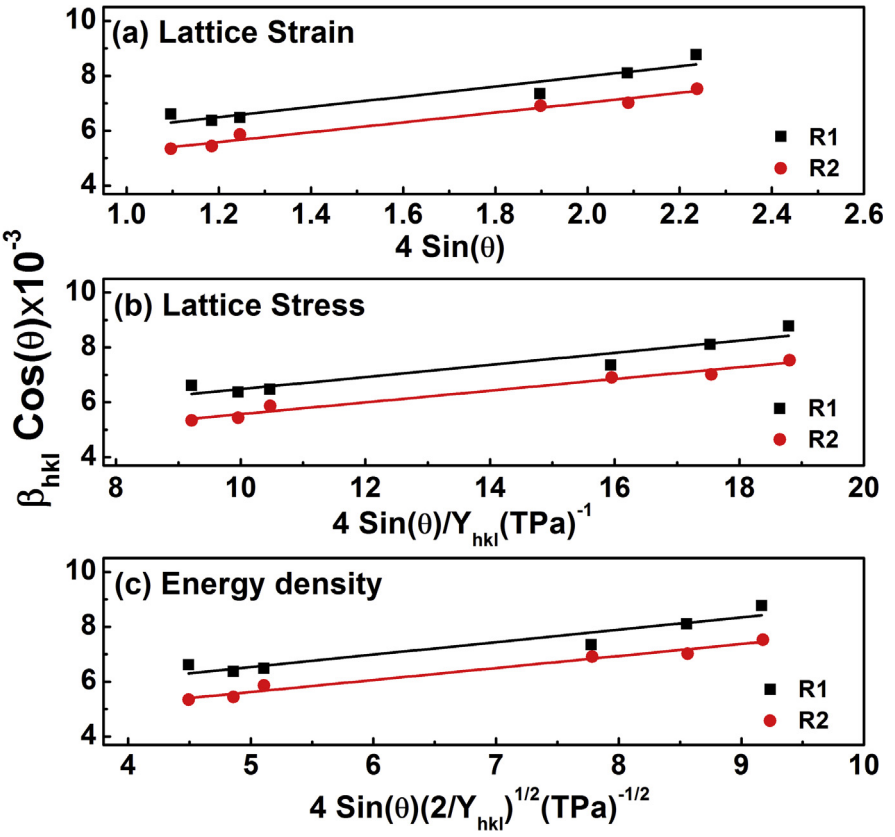

Fig. 6. W-H plots with linear fitting based on (a) UDM for strain approximation (b) USDM for stress approximation, (c) UDEDM for energy density.

used to approximate the crystal size. In the above-described models, lattice strain, stress and energy density were determined within certain approximation (Table 2). It clearly show the decrease in strain value with the increase in crystal size from R1 to R2; and hence the decrease in stress and energy values too. The crystallite size for R1 and R2 obtained using these models were in good agreement with the average size calculated after Rietveld refinement, as listed in Table 2.

3.4. Optical properties

Fig. 7 shows the graph between absorbance and wavelength for R1 and R2 samples. The Kubelka-Munk (K-M) model was used to determine the band gap based on Eq. (7).

$$F(R) = \frac{(1-R)^2}{2R} \tag{7}$$

where *F(R)* is K-M function and *R* is reflectance [33]. Graph is plotted between $(F(R)h\nu)^2$ and $h\nu$ for two samples, where intercept give value of energy band gap (shown

https://doi.org/10.1016/j.heliyon.2018.e00594

Table 2. Crystal size and simulated parameters through various W-H models for R1 and R2.

Sample name	Crystal size D(nm)	W-H method					
		UDM		USDM		UDEDM	
		D(nm)	$\varepsilon \times 10^{-3}$	D(nm)	σ (MPa)	D(nm)	u(kJm^{-3})
R1	23 ± 1	35 ± 4	1.9 ± 0.3	35 ± 4	221 ± 35	35 ± 4	203 ± 5
R2	26 ± 1	44 ± 3	1.8 ± 0.1	44 ± 3	213 ± 16	44 ± 3	185 ± 1

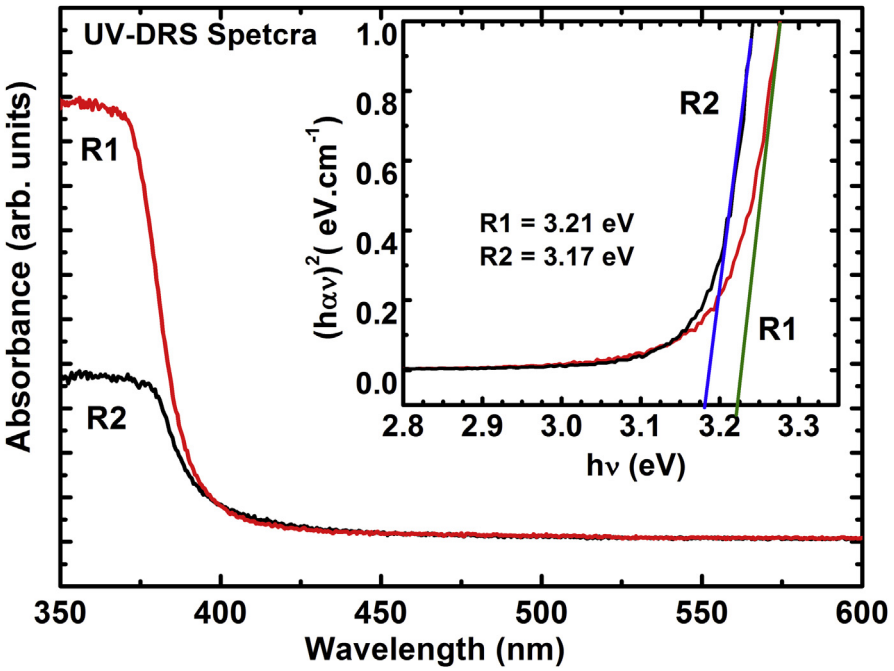

Fig. 7. UV-DRS spectra of R1 and R2 samples. Inset shows the graph between $(F(R)\ h\nu)^2$ and $h\nu$ based on K-M model.

in inset of Fig. 7). The band gap was found to be 3.21 eV for R1 and 3.17 eV for R2. Small difference in the band gap was due to size parameter.

3.5. Evaluation of vacancies and local atomic structure

The synchrotron based XAS technique was used to evaluate the vacancies present in R1 and R2. In this technique, transition of core electron took place on absorbing photon energy and these transitions were governed by dipole selection rules [34]. Fig. 8a ascribed the normalized total electron yield (TEY) NEXAFS spectra at O K- edge giving information about transitions from O 1s state to unoccupied $2p_{\Pi}$ and $2p_{\sigma}$ orbitals. We adjusted the intensity to 0 at 530 eV. Four features A1-A4 was located at 537, 539.8, 542.5, 545.5 eV, respectively. The spectral feature A1, A2 in the energy range 536−540 eV corresponds to the O 2p hybridization with

https://doi.org/10.1016/j.heliyon.2018.e00594

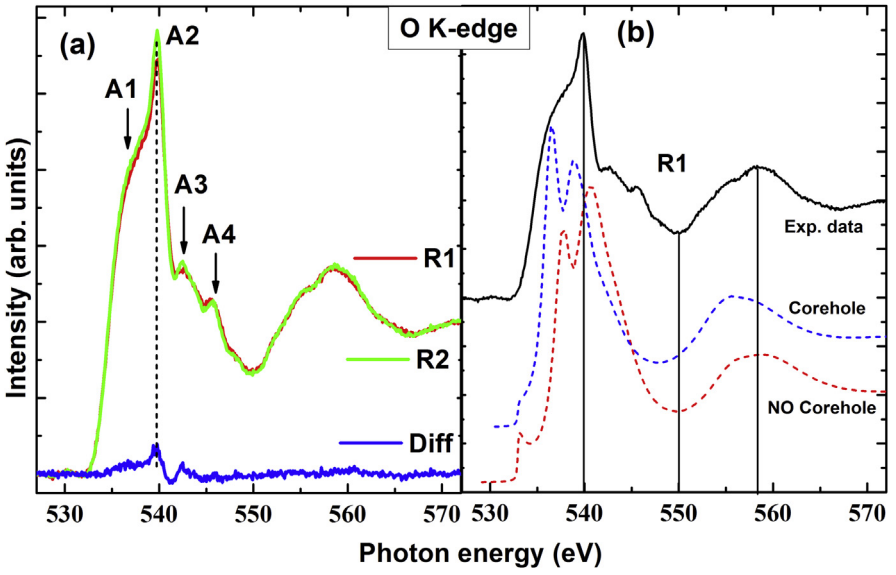

Fig. 8. (a) Normalized NEXAFS spectra at O *K*-edge for R1 and R2, (b) simulated data by using core hole effect and no-core hole effect for R1. Solid lines represent a close match of the experimental and simulated data when no-core hole potential was considered.

Zn 3*d*4*s* states following the selection rules. Features A3, A4 in the energy range 541−549 eV were due to O 2*p* state hybridization with Zn 4*p* state. Beyond this energy, the spectral features were due to hybridization of O 2*p* with Zn higher extended states. In Fig. 8a, the blue line represents the difference spectra of the two samples, which is almost a straight line. Thus all the spectral features of R1 and R2 matched with each other.

For detailed investigation, we used FEFF9.05 code and performed analysis for both core hole and no-core hole potential in order to have an agreement between experiment and theory as shown in Fig. 8b. Simulation done with no-core hole effect matched well (except at the peak A1) with the experiment (shown for R1 sample). The intensity at peak A1 found to be suppressed in experimental spectra in both samples and this suppression could be attributed to the presence of defects/vacancies in the structure. These defect states include Zn-vacancy, O-vacancy and Zn-interstitial [35]. Hsu *et al.* [36] reported the formation of oxygen vacancies at the pre-edge of Zn *K*- edge for ZnO that can be correlated to the room temperature ferromagnetism (RTFM). In order to see insight nature of defects, we performed simulation by introducing oxygen defects and zinc defects into ZnO under the same conditions as for ZnO, shown in Fig. 9. When zinc vacancy was created, no change was observed in the intensity of peak A1 (Fig. 9b and d). Whereas, on introduction of oxygen vacancy, the suppression of peak A1 occurred and simulated data show a trend similar to experiment as clearly seen in Fig. 9a and c. It was therefore concluded that prepared samples have oxygen-vacancy defects in the structure. Fig. 10 shows Zn

https://doi.org/10.1016/j.heliyon.2018.e00594

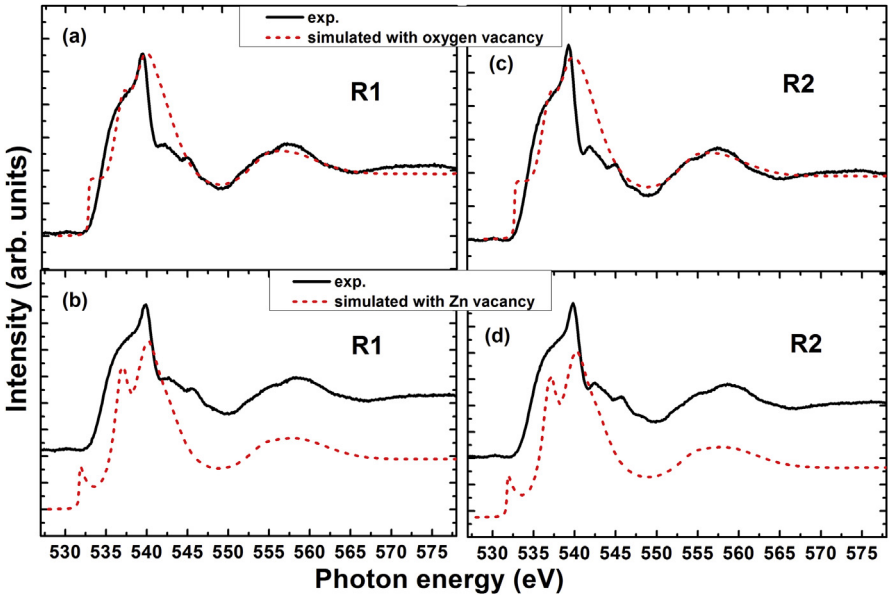

Fig. 9. Comparison between experiment and simulated data in presence of oxygen vacancy (a, c) and Zn vacancy (b, d) for both samples by taking no-core hole effect. Creation of oxygen vacancy gives a better match to the experiment.

$L_{3,2}$ −edge spectral features, which indicate the transition between various energy states. As we know that in ZnO, 3*d* states are fully occupied, thus Zn L_3 -edge is very sensitive to electron transitions from 2*p* to 4*s*4*d* states being followed by Mott-selection rules [34]. In Fig. 10a, spectral feature B1 (1022.6 eV) has contribution from Zn 4*s* state, whereas B2 (1027.1 eV), B3 (1031.6 eV) were followed up by

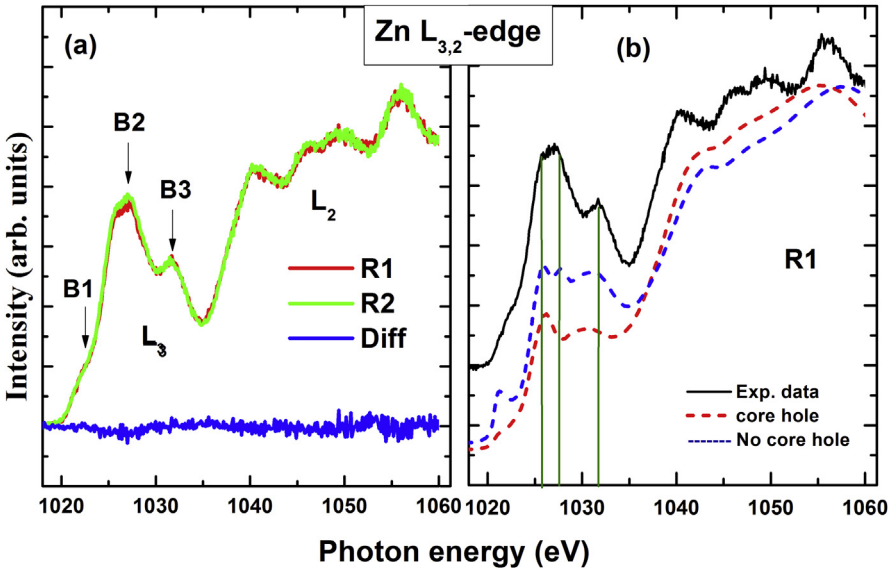

Fig. 10. (a) Normalized NEXAFS spectra at Zn $L_{3,2}$-edge of ZnO, where blue line represents the difference in features, (b) comparison between experimental and simulated data by using core hole effect and no-core hole effect for R1.

https://doi.org/10.1016/j.heliyon.2018.e00594

4*d* transition states and higher transition is due to multiple overlapping of bands [37]. Further simulation using FEFF9.05 was carried by considering core-hole and no-core hole effects to correlate the experimental results (Fig. 10b). Data simulated with no-core hole potential gave satisfactory agreement in both experimental and theoretical results as shown in Fig. 11a and b. Both R1 and R2 have almost same NEXAFS spectral features, which show that ZnO with different morphologies exhibit same transitions.

To determine the local atomic structure around absorbing atom, EXAFS measurements at Zn *K*- edge were performed. Data was analyzed using FEFF9.05 code. Fig. 12a and b represents normalized EXAFS spectra of R1 and R2 and the XANES (X-ray absorption near-edge structure) spectra at Zn *K*−edge for both samples. The XANES spectrum was considerably same for both. The spectral feature marked with dotted lines represents the transition from 1*s* to 4*p* states. Fig. 12c show the Zn k^2-weighted EXAFS oscillation spectrum of ZnO nanoparticles. $k^2\chi(k)$ plotted as a function of wave vector *k,* which provides thorough facts about the atomic environment of lattice. Further simulation of Fourier Transform (FT) EXAFS function was performed through FEFF9.05 Artemis, which shows two prominent peaks corresponding to Zn-O and Zn-Zn bond spacing (Fig. 12d). The coordination number (N), bond distance (R) and Debye-Waller factor (σ^2) has been considered as fitting parameters. The amplitude (S_0^2) calculated from the metal-foil data and absorption edge energy shift (ΔE_0) was kept 0.72 and 4.78 eV, respectively. Data range taken in *k*-space was 3−10 $\mathring{A}^{-1}$ and the fitting was done in R-space within 1.0−3.7 $\mathring{A}$ using hanning window. In the simulation, a coordination of first 4 O atoms and 12 Zn second nearest atoms were taken into consideration. The best fit parameters have been shown in Table 3, compared with the reported data [38, 39]. Various oscillations in

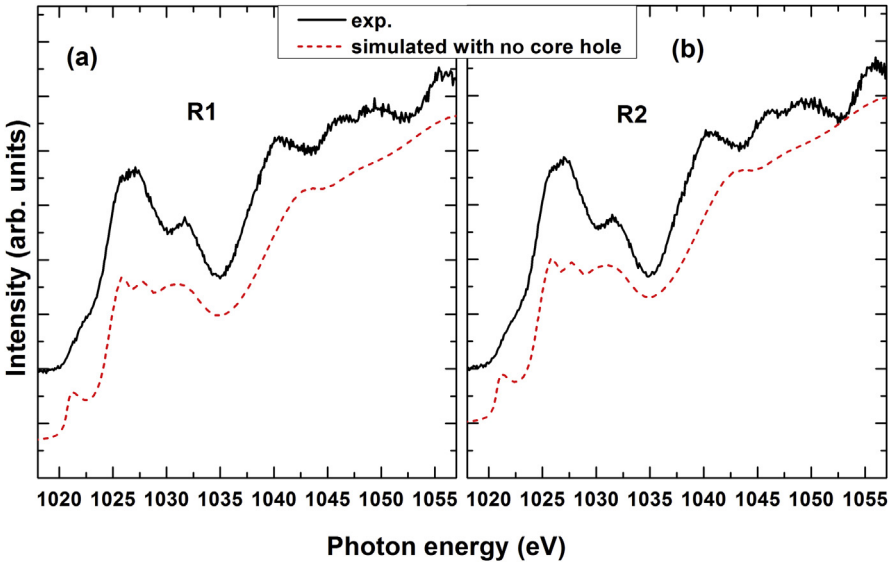

Fig. 11. Simulation performed with no- core hole potential for R1 and R2.

https://doi.org/10.1016/j.heliyon.2018.e00594

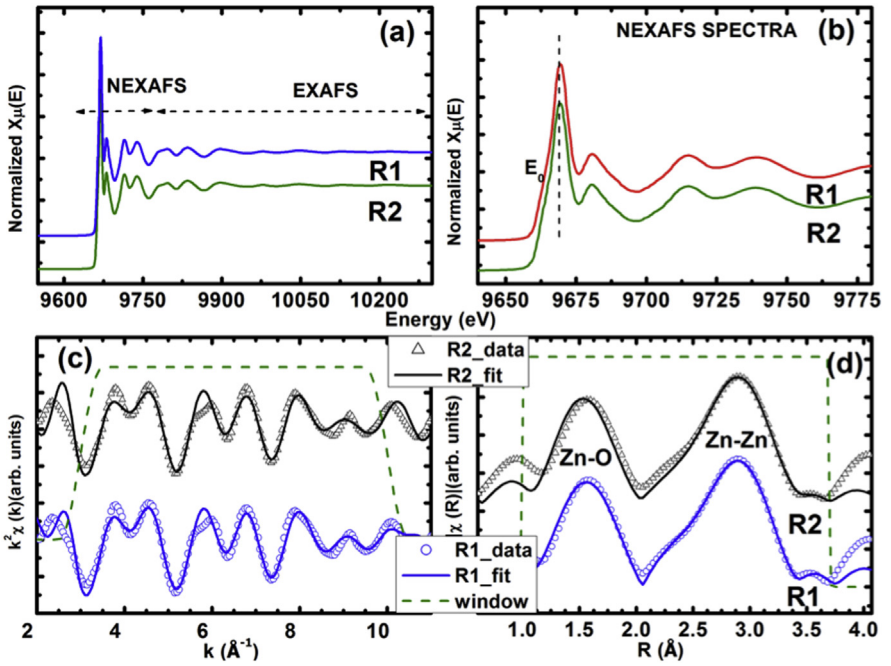

Fig. 12. (a) Normalized Xμ(E) spectra at Zn *K*-edge, (b) XANES spectrum around Zn K- edge, (c) $k^2\chi(k)$ weighted EXAFS oscillations (open symbols) along with their best fits (solid lines) in the region k = 3−10 $Å^{-1}$ (marked with dotted line window), (d) Radial distribution obtained by Fourier Transform of EXAFS oscillations (open symbols) and their best fits (solid line).

Table 3. The analyzed results of EXAFS spectra of R1 and R2. N is the coordination number, R is bond distance and σ^2 is Debye-Waller factor. The amplitude (S_0^2) and absorption edge energy shift (ΔE_0) is fixed as 0.72 and 4.78 eV, respectively. The simulated data is compared with reported data [38, 39].

Pair	R1			R2			N	Ref [38]	Ref [39]
	N	R (Å)	σ^2 ($Å^2$)	N	R (Å)	σ^2 ($Å^2$)		R (Å)	R (Å)
Zn-O(4)	4	1.988	0.002	4	1.975	0.017	4	1.970	1.942
Zn-Zn(12)	12	3.176	0.001	12	3.268	0.014	12	3.250	3.226

$k^2\chi(k)$ curves (Fig. 12c) exhibited similar trend, which revealed Zn-ions coordination to be same in both samples. Fig. 12d represents the radial distribution function at Zn *K*-edge in terms of FT of EXAFS oscillations. Thus from the EXAFS spectra, it was inferred that samples have similar spectral features and thus have same local atomic structure.

4. Conclusion

Effect of different synthesis environment on physical, morphological and electronic properties was accessed. XRD and Raman analysis concluded that hydrothermal

https://doi.org/10.1016/j.heliyon.2018.e00594

synthesis has improved crystallinity. It also indicated the formation of long-range order ZnO lattice along with 3D structure in hydrothermal synthesis process. The results of modified W-H equations indicated lowering of strain, stress and energy density values with the increasing crystallite size. From FE-SEM, the growth process of two differently attained morphologies was put forward giving relevant facts about the formation of ZnO nanostructure and μ- flower. Theoretical study of X-ray absorption spectroscopy further revealed the presence of oxygen vacancies in both the samples, apart from their different morphology. Moreover, as the morphology changed on adopting two different synthesis routes, their local electronic/atomic structure tends to follow the similar behavior as predicted from density functionally theory (DFT) calculations (FEFF9.05), which might be due to the small difference in crystallite size in both cases. The synthesized material via hydrothermal technique is better for potential applications in spintronics/optoelectronic devices.

Declarations

Author contribution statement

Richa Bhardwaj: Conceived and designed the experiments; Performed the experiments; Analyzed and interpreted the data; Wrote the paper.

Amardeep Bharti: Performed the experiments; Wrote the paper.

Jitendra Pal Singh: Performed the experiments.

Keun Hwa Chae: Analyzed and interpreted the data; Contributed reagents, materials, analysis tools or data.

Navdeep Goyal: Conceived and designed the experiments; Analyzed and interpreted the data; Contributed reagents, materials, analysis tools or data.

Sanjeev Gautam: Conceived and designed the experiments; Analyzed and interpreted the data; Contributed reagents, materials, analysis tools or data; Wrote the paper.

Funding statement

Richa Bhardwaj was supported by the INSPIRE fellowship (IF150139). This Research is supported by UGC-BSR [F.30-94/2015(BSR)] research project.

Competing interest statement

The authors declare no conflict of interest.

https://doi.org/10.1016/j.heliyon.2018.e00594

Additional information

No additional information is available for this paper.

Acknowledgements

Authors are thankful to Dr. Fouran Singh (Inter University Accelerator Center, New Delhi) for Raman measurements.

References

[1] J. Ge, B. Tang, L. Zhuo, Z. Shi, A rapid hydrothermal route to sisal-like 3D ZnO nanostructures via the assembly of CTA + and $Zn(OH)_4^{2-}$: growth mechanism and photoluminescence properties, Nanotechnology 17 (2006) 1316−1322.

[2] X. Wang, J. Song, J. Liu, Z.L. Wang, Direct-current nanogenerator driven by ultrasonic waves, Science 316 (2007) 102−105.

[3] T. P. Chou, Q. Zhang, G.E. Fryxell, G.Z. Cao, Hierarchically structured ZnO film for dye-sensitized solar cells with enhanced energy conversion efficiency, Adv. Mater. 19 (18) (2007) 2588−2592.

[4] F. Qingfei, L. Qi, Z. Meili, F. Ximei, Z. Zuowan, Z. Chaoliang, Preparation and photocatalytic activities of 3D flower-like CuO nanostructures, J. Semiconduct. 37 (8) (2016) 083002.

[5] Liang-Shu Zhong, Jin-Song Hu, An-Min Cao, Qiang Liu, Wei-Guo Song, Li-Jun Wan, 3D flowerlike ceria micro/nanocomposite structure and its application for water treatment and CO removal, Chem. Mater. 19 (7) (2007) 1648−1655.

[6] A.B. Djurišić, A.M.C. Ng, X.Y. Chen, ZnO nanostructures for optoelectronics: material properties and device applications, Prog. Quant. Electron. 34 (4) (2010) 191−259.

[7] A. Quintana, A. Gómez, Maria D. Baró, S. Suriñach, E. Pellicer, J. Sort, Self-templating faceted and spongy single-crystal ZnO nanorods: resistive switching and enhanced piezoresponse, Mater. Des. 133 (2017) 54−61.

[8] A. Tamvakos, K. Korir, D. Tamvakos, D. Calestani, G. Cicero, D. Pullini, NO_2 gas sensing mechanism of ZnO thin-film transducers: physical experiment and theoretical correlation study, ACS Sens. 1 (4) (2016) 406−412.

[9] J. Saffari, N. Mir, D. Ghanbari, K. Khandan-Barani, A. Hassanabadi, M.R. Hosseini-Tabatabaei, Sonochemical synthesis of Fe_3O_4/ZnO magnetic

https://doi.org/10.1016/j.heliyon.2018.e00594

nanocomposites and their application in photo-catalytic degradation of various organic dyes, J. Mater. Sci. Mater. Electron. 26 (12) (2015) 9591–9599.

[10] G. Byzynski, C. Melo, D.P. Volanti, M.M. Ferrer, A.F. Gouveia, C. Ribeiro, J. Andrés, E. Longo, The interplay between morphology and photocatalytic activity in ZnO and N-doped ZnO crystals, Mater. Des. 120 (2017) 363–375.

[11] M. Law, L.E. Greene, J.C. Johnson, R. Saykally, P. Yang, Nanowire dye-sensitized solar cells, Nat. Mater. 4 (2005) 455–459.

[12] S.D. Lee, Sang-Hun Nam, Myoung-Hwa Kim, Y.D. Kim, Jin-Hyo Boo, Synthesis of ZnO nanoparticles by spray-pyrolysis method and their photocatalytic effect, in: 3rd International Nanoelectronics Conference (INEC), 2010, pp. 572–573.

[13] Y.T. Chung, M.M. Ba-Abbad, A.W. Mohammad, N.H.H. Hairom, A. Benamor, Synthesis of minimal-size ZnO nanoparticles through sol–gel method: Taguchi design optimisation, Mater. Des. 87 (2015) 780–787.

[14] A. Hassanpour, N. Bogdan, J.A. Capobianco, P. Bianucci, Hydrothermal selective growth of low aspect ratio isolated ZnO nanorods, Mater. Des. 119 (2017) 464–469.

[15] Y. Bao, C. Wang, Jian-zhong Ma, Morphology control of ZnO microstructures by varying hexamethylenetetramine and trisodium citrate concentration and their photocatalytic activity, Mater. Des. 101 (2016) 7–15.

[16] N. Islavath, D. Das, S.V. Joshi, E. Ramasamy, Seed layer-assisted low temperature solution growth of 3D ZnO nanowall architecture for hybrid solar cells, Mater. Des. 116 (2017) 219–226.

[17] Y. Wang, Q. Ma, H. Jia, Z. Wang, One-step solution synthesis and formation mechanism of flower-like ZnO and its structural and optical characterization, Ceram. Int. 42 (2016) pp.10751–10757.

[18] A. Khorsand Zak, W.H. Abd. Majid, M.E. Abrishami, Ramin Yousefi, X-ray analysis of ZnO nanoparticles by Williamson–Hall and size–strain plot methods, Solid State Sci. 13 (1) (2011) 251–256.

[19] Xiaodong Si, Yongsheng Liu, Xinfang Wu, Wei Lei, Juan Xu, Wenlong Du, Tao Zhou, Jia Lin, The interaction between oxygen vacancies and doping atoms in ZnO, Mater. Des. 87 (2015) 969–973.

[20] S. Gautam, S. Kumar, P. Thakur, K.H. Chae, Ravi Kumar, B.H. Koo, C.G. Lee, Electronic structure studies of Fe-doped ZnO nanorods by X-ray absorption fine structure, J. Phys. D Appl. Phys. 42 (2009) 175406.

 https://doi.org/10.1016/j.heliyon.2018.e00594

[21] F.A. Akgül, Influence of Ti doping on ZnO nanocomposites: synthesis and structural characterization, Composites Part B 91 (2016) 589−594.

[22] J.P. Singh, S.O. Won, W.C. Lim, Ik-Jae Lee, K.H. Chae, Electronic structure studies of chemically synthesized $MgFe_2O_4$ nanoparticles, J. Mol. Struct. 1108 (2016) 444−450.

[23] J. Rodríguez-Carvajal, Recent advances in magnetic structure determination by neutron powder diffraction, Phys. B Condens. Matter 192 (1993) 55−69.

[24] John J. Rehr, Joshua J. Kas, Fernando D. Vila, Micah P. Prange, Kevin Jorissen, Parameter-fre calculations of X-ray spectra with FEFF9.05, Phys. Chem. Chem. Phys. 12 (2010) 5503−5513.

[25] John J. Rehr, Theory and calculations of X-ray spectra: XAS, XES, XRS, and NRIXS, Radiat. Phys. Chem. 75 (2006) 1547−1558.

[26] J.U. Brehm, M. Winterer, H. Hahn, Synthesis and local structure of doped nanocrystalline zinc oxides, J. Appl. Phys. 100 (2006) 064311.

[27] P. Soundarrajan, M. Sampath, T. Logu, K. SethuRaman, K. Ramamurthi, Doping introduce nucleation site barrier in ZnO nano/micro rod arrays film grown by chemical bath deposition, Mater. Lett. 162 (2016) 191−194.

[28] B. Pal, P.K. Giri, Defect mediated magnetic interaction and high T_c ferromagnetism in Co doped ZnO nanoparticles, J. Nanosci. Nanotechnol. 11 (2011) 1−8.

[29] D. Das, P. Mondal, Photoluminescence phenomena prevailing in *c-axis* oriented intrinsic ZnO thin films prepared by RF magnetron sputtering, RSC Adv. 4 (2014) 35735−35743.

[30] G. Amin, M.H. Asif, A. Zainelabdin, S. Zaman, O. Nur, M. Willander, Influence of pH, precursor concentration, growth time, and temperature on the morphology of ZnO nanostructures grown by the hydrothermal method, J. Nanomater. 269692 (2011) 9.

[31] Y. Sun, L. Wang, X. Yu, K. Chen, Facile synthesis of flower-like 3D ZnO superstructures via solution route, CrystEngComm 14 9 (2012) 3199−3204.

[32] S. Cho, Ji-Wook Jang, J.S. Lee, Kun-Hong Lee, Exposed crystal face controlled synthesis of 3D ZnO superstructures, Langmuir 26 (17) (2010) 14255−14262.

[33] P. Kubelka, New contributions to the optics of intensely light-scattering materials: I, J. Opt. Soc. Am. 38 (1948) 448−457.

 https://doi.org/10.1016/j.heliyon.2018.e00594

[34] N.F. Mott, The basis of the electron theory of metals, with special reference to the transition metals, Proc. Phys. Soc. Lond A 62 (7) (1949) 416−422.

[35] K. Johnston, Martin O. Henry, D. McCabe, E. McGlynn, M. Dietrich, E. Alves, M. Xia, Identification of donor-related impurities in ZnO using photoluminescence and radiotracer techniques, Phys. Rev. B 73 (16) (2006) 165212.

[36] H.S. Hsu, J.C.A. Huang, Y.H. Huang, Y.F. Liao, M.Z. Lin, C.H. Lee, J.F. Lee, S.F. Chen, L.Y. Lai, C.P. Liu, Evidence of oxygen vacancy enhanced room-temperature ferromagnetism in Co-doped ZnO, Appl. Phys. Lett. 88 (2006) 242507.

[37] J.W. Chiou, K.P. Krishna Kumar, J.C. Jan, H.M. Tsai, C.W. Bao, W.F. Pong, F.Z. Chien, M.-H. Tsai, I.-H. Hong, R. Klauser, J.F. Lee, J.J. Wu, S.C. Liu, Diameter dependence of the electronic structure of ZnO nanorods determined by X-ray absorption spectroscopy and scanning photoelectron microscopy, Appl. Phys. Lett. 85 (2004) 3220−3222.

[38] J. Segura-Ruiz, G. Martínez-Criado, M.H. Chu, S. Geburt, C. Ronning, Nano-X-ray absorption spectroscopy of single co-implanted ZnO nanowires, Nano Lett. 11 (12) (2011) 5322−5326.

[39] Eun-Suk Jeong, Hyo-Jong Yu, Yong-Jin Kim, Gyu-Chul Yi,Yong-Dae Choi, Sang-Wook Han, Local structural and optical properties of ZnO nanoparticles, J. Nanosci. Nanotechnol. 10 (2010) 3562−3565.

https://doi.org/10.1016/j.heliyon.2018.e00594